Journal of *Marine Science and Engineering*

MDPI

Article

Experimental Investigation on the Hydraulic Characteristics of Self-Rotating Flood Barrier

Jooyeon Lee [1], Byoungjoon Na [2] and Sang-Ho Oh [3,*]

[1] Ocean Space Development and Energy Research Department, Korea Institute of Ocean Science and Technology, Busan 49111, Republic of Korea; leejy@kiost.ac.kr
[2] Department of Civil Engineering, Kumoh National Institute of Technology, Gumi 39177, Republic of Korea; byoungjoon.na@kumoh.ac.kr
[3] Department of Civil Engineering, School of Smart and Green Technology, Changwon National University, Changwon 51140, Republic of Korea
* Correspondence: coast.oh@gmail.com; Tel.: +82-55-213-3779

Abstract

This study investigated the hydraulic characteristics of a self-rotating flood barrier (SRFB) by performing laboratory experiments. The SRFB is proposed as a secure solution to withstand both waves and sudden water level rise, thereby protecting the coastal area behind it. The SRFB is designed to rotate and rise automatically by buoyancy when the water level exceeds a certain threshold or waves start to overtop the crest level of the caisson, where the barrier is enclosed. The barrier begins to rise when the chamber is filled with enough water for the buoyancy force to exceed its own weight. The performance of the structure was tested under various regular wave conditions at different water depths. Pressure transducers were placed along the front face of the barrier to measure the wave pressures acting on it. The barrier's angular displacement was also identified using synchronized video footage during the measurements. The results showed that the overall magnitude of the measured pressures increased with water depth due to the larger volume of water inflow from overtopping waves. During the rise in the barrier, the pressure profiles dynamically varied with the rotation angle as the pattern of water flow into the chamber changed depending on the test cases. Analysis results showed how the pressures are distributed along the barrier at the moment of peak wave force. These findings would provide fundamental information for estimating design wave forces on the structure.

Keywords: self-rotating flood barrier; buoyancy-driven seawall; water level rise; wave pressure; physical experiment

Academic Editor: Eugen Rusu

Received: 4 July 2025
Revised: 30 July 2025
Accepted: 6 August 2025
Published: 11 August 2025

Citation: Lee, J.; Na, B.; Oh, S.-H. Experimental Investigation on the Hydraulic Characteristics of Self-Rotating Flood Barrier. *J. Mar. Sci. Eng.* **2025**, *13*, 1542. https://doi.org/10.3390/jmse13081542

1. Introduction

Coastal areas are vulnerable to flooding, erosion, and damage to infrastructure and property caused by high water levels and waves, which eventually result in significant economic and social losses. Moreover, due to sea level rise and changes in storm characteristics associated with climate change, severe storms are likely to become more frequent in coastal regions [1,2]. This situation poses a serious threat, particularly to low-lying, densely populated, and developed coastal areas. Therefore, there is an urgent need to protect these coastal regions from the risks associated with extreme storms.

The traditional method of dealing with high water level rise or large waves involves constructing coastal structures such as seawalls or levees. These rigid structures are permanently standing on the ground and have a fixed height and shape. However, they

inherently separate land and sea spaces and obstruct landscape views. Given the increasing demand for waterfront access and the utilization of coastal spaces, there are limitations to raising the crest height of seawalls or levees, especially in commercially developed regions with strong tourism and leisure industries. To address this issue, movable walls have been developed [3,4], which can adjust their height and shape according to water levels and wave conditions. These movable walls are selectively closed only during extreme storm events, allowing for the free passage of people and traffic and unobstructed ocean views during ordinary conditions. This adaptability enables the structures to perform different functions depending on the situation. For instance, a movable wall designed to prevent wave overtopping during stormy conditions can serve as a tourist deck in normal times.

The basic concept of a movable wall is similar to adaptive water level control systems often used in rivers, such as flood gates [5,6] or storm surge barriers [7–11]. Although these systems are often used as control structures on rivers or reservoirs, the underlying concepts and mechanics are very similar. Flood gates optimally adjust the water level in a waterway to either store water for various uses or prevent flooding during high-water events. Storm surge barriers are a specific type of flood gate designed to prevent the inflow of water into the protected areas during severe storm surges. Larger versions of these facilities are primarily operated by hydraulic oil systems, which use pressurized oil to move the gate or barrier up and down according to the desired water level.

On the other hand, there are movable flood gates or barriers that utilize buoyancy instead of hydraulic oil systems by changing their buoyant force in water [12,13]. One method of using buoyancy involves placing an air chamber within the barrier. By inflating or deflating these air chambers, the barrier can change its density and adjust its position relative to the water surface. Another approach is to install a water container inside the barrier. By filling or emptying the water container, the barrier can float or sink depending on its buoyant force relative to water [14,15]. Due to their buoyancy-dependent flexible nature, these types of movable barriers can be designed in various shapes and sizes to meet the flow characteristics and requirements of specific applications.

There are still a few examples of buoyancy-activated flood barriers. One realization is the self-closing flood barrier [16,17]. In normal conditions, it is enclosed in a narrow rectangular chamber beneath the ground, but during an emergency, it rises by buoyancy to prevent inundation. Another example is the flap-type barrier named Neorise, developed by Hitachi Zosen Corporation, Japan [18]. The Neorise consists of a flap gate positioned between the side walls, equipped with a counterweight to control the rotational movement of the gate depending on the water level. However, while these structures are generally resistant to flooding caused by rising water levels, they are structurally vulnerable in the event of relatively high waves.

In this study, a new type of flood barrier called the self-rotating flood barrier (SRFB) is proposed that can securely withstand the impact of waves. This structure resembles a radial gate, but its float and sink mechanisms are operated solely by buoyancy, eliminating the need for external power or manual intervention. Additionally, the end of the gate is shaped like a recurved wall to effectively reduce the amount of wave overtopping [19,20]. When there is no threat of waves or unexpected water level rise, the entire structure is enclosed below the ground level, which is advantageous for preserving views and landscapes for residents and tourists. Hence, it is a kind of buoyancy-driven seawall that is installed on land adjacent to the shore to prevent coastal flooding only when needed.

This paper mainly presents the results of an experimental study on this structure, conducted in a wave flume. The paper is organized as follows. In the next section, the outline of the self-rotating flood barrier is described. Section 3 explains the details of the experimental model and setup. Section 4 elucidates the experimental results on the

model's behavior under different water depths and wave conditions. Finally, conclusions are presented in Section 5.

2. Concept and Working Principle of Self-Rotating Flood Barrier

The self-rotating flood barrier (SRFB) is designed to flexibly respond to both overtopping waves and unusually high water levels. As shown in Figure 1, SRFB consists of a flood barrier that acts as a float and a caisson that stores the barrier in normal times. The front face of the barrier has an arc shape, effectively transmitting wave loads to the hinge. As depicted in Figure 2, the caisson contains two chambers. When the water level in the front chamber rises above the top of the internal waterway, water enters the rear chamber (Figure 2a). The front chamber functions as a buffer zone, preventing the barrier from rising prematurely until the incoming water surpasses the top of the internal waterway. If waves overtop the crest of the vertical front wall, water also enters through the external waterway (Figure 2b). Once the water in the rear chamber is sufficient to have enough buoyancy to overcome the weight of the barrier, the barrier begins to rotate around the hinge and rise, as illustrated in Figure 3. In short, the SRFB operates solely through buoyancy and does not require external power, such as hydraulics or electricity. In its resting state, the flood barrier is enclosed in the rear chamber but will automatically rise if the hinterland is at risk of flooding.

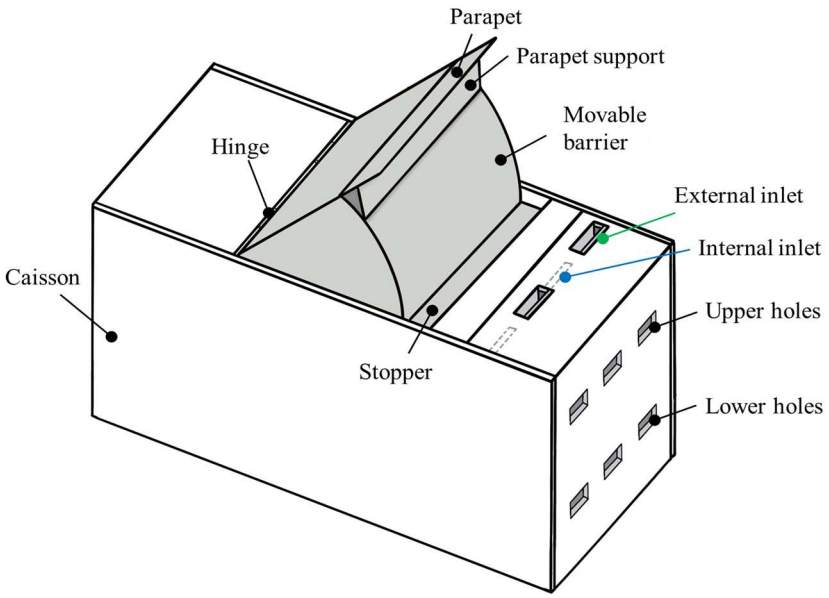

Figure 1. Bird-eye view of the self-rotating flood barrier.

It is noteworthy that once the flood barrier begins to rise, a gap opens between the front face of the barrier and the top of the caisson, allowing the overtopping water to hit the rising barrier and then fall through the gap into the rear chamber. Before the arch-shaped barrier is fully erected and the stopper touches the top inner surface of the caisson, a space is created in front of the arch-shaped barrier surface, so that the overtopped water hitting the barrier naturally falls downward, accumulating in the rear chamber. This contribution of the volume of water has no negative effect on the rise of the barrier, but enables the barrier to rise faster because the water volume falling through the gap is larger than that from the external inlets. Meanwhile, the thin protruding parapet located at the top of the barrier functions as a recurved wall, reducing the volume of overtopping waves. The movement of the barrier is restricted upward by a stopper located near its base. Without

this stopper, the barrier would rise too far and tilt backward, especially when subjected to relatively high waves.

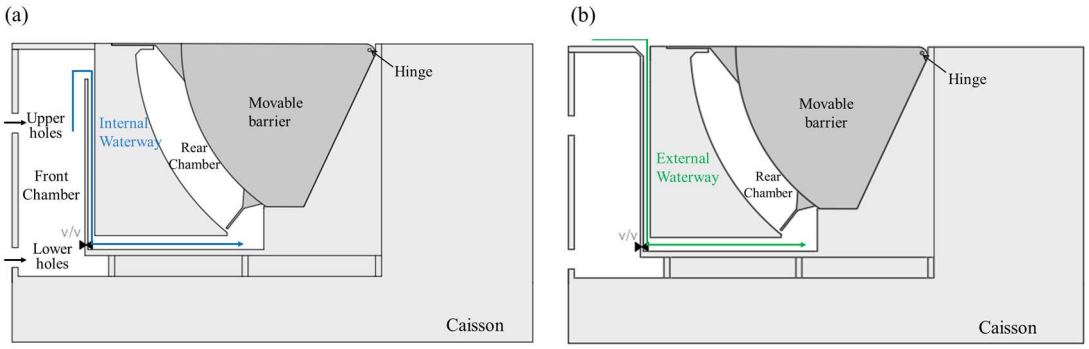

Figure 2. Conceptual illustration of the two methods for filling the rear chamber with water. (**a**) The water can enter the rear chamber through the internal waterway if the water level in the front chamber exceeds the threshold. (**b**) The water can enter the rear chamber through the external waterway when waves overtop the caisson or the water level exceeds the caisson crest height.

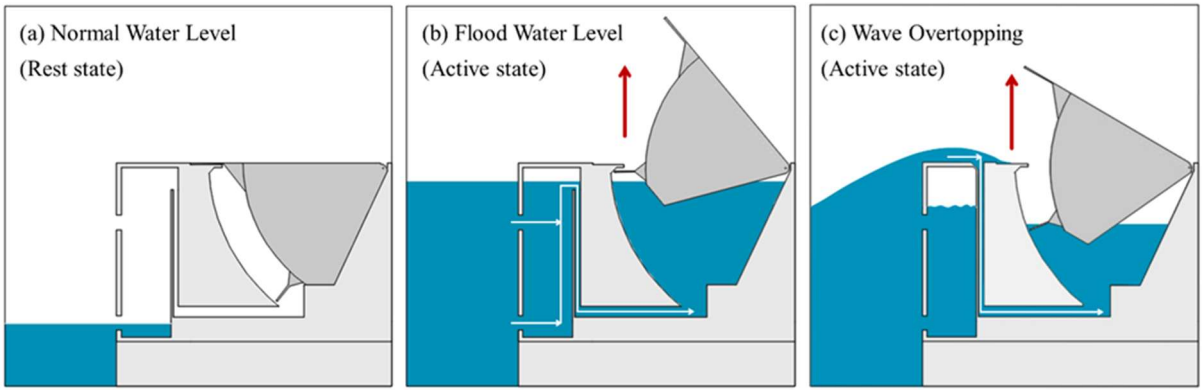

Figure 3. Behavior of the flood barrier during rest and active states. (**a**) The barrier does not rise when the water level is lower than the threshold (the height of the internal inlet). (**b**) The barrier rises as the water enters the rear chamber through the internal waterway due to the higher water level than the threshold. The red arrow indicates that the SRFB rises upward as the water level in the rear chamber rises. (**c**) The barrier rises as the water enters the rear chamber through the external waterway, as waves overtop the caisson. In this condition, the water level in the front chamber can be even lower than the height of the internal inlet. The red arrow indicates that the SRFB rises upward as the water level in the rear chamber rises.

At the bottom of both internal and external waterways, a non-return valve is installed to allow water in the rear chamber to flow out when the water level outside falls below the elevation of the waterway bottom. As shown in Figure 2, the front wall of the caisson has lower holes that permit water to flow in and out of the first chamber. When the water level in front of the front chamber drops, the water in the rear chamber can naturally drain through the front chamber to the outside via the valve, since the elevation of the lower holes is slightly lower than the floor of the rear chamber. This process reduces the buoyancy force acting on the barrier, causing it to naturally lower back to its original position.

3. Experiments

A series of experiments was carried out to verify the performance of the SRFB to ensure it operates well by buoyancy and to evaluate characteristics of wave pressure acting on the structure. The experiments were performed in a wave flume 50 m long, 1.6 m high, and 1.2 m wide [21]. Figure 4 provides a schematic diagram of the wave flume, showing the

locations of the wave gauges and the SRFB model. A piston-type wave maker is operated by the AwaSys 7 software [22], which enables active absorption of the energy of reflected waves.

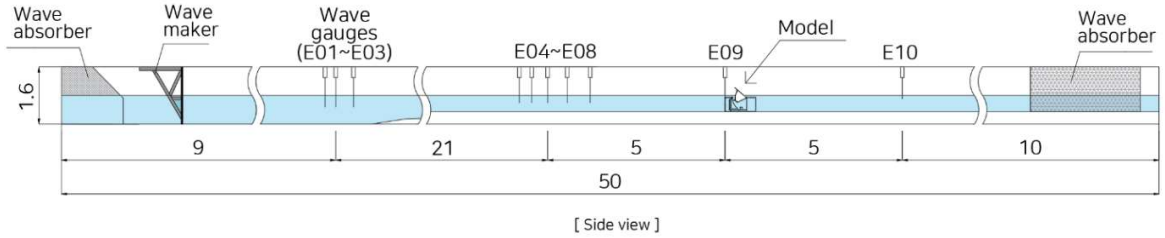

Figure 4. Schematic diagram of the wave flume showing the experimental setup (unit: m).

3.1. Design and Manufacture of the SRFB Model

The SRFB model was manufactured using polycarbonate (PC) plates. The caisson containing the flood barrier was 0.52 m high and 0.4 m wide. Although the model was not built considering the prototype structure of the SRFB, the experimental scale can be assumed to be approximately 1:10 to 1:20, considering the dimensions of the likely prototype structure. Since the wave flume is 1.2 m wide, a dummy rectangular box was placed to occupy the remaining 0.8 m of width after the SRFB model was installed in the flume. The radius of the arch-shaped surface was 0.31 m, and the maximum angle of rotation was 50°. When the barrier was fully raised in the active state, the top of the barrier reached 0.85 m high from the bottom of the caisson. All elements of the caisson were made to be watertight, preventing water ingress except through the internal and external inlets. As illustrated in Figure 5, the front of the caisson had a total of six rectangular holes, with the bottom three at a height of 0.145 m from the caisson bottom and the top three at a height of 0.37 m. In the following, any height refers to the height measured from the bottom of the caisson.

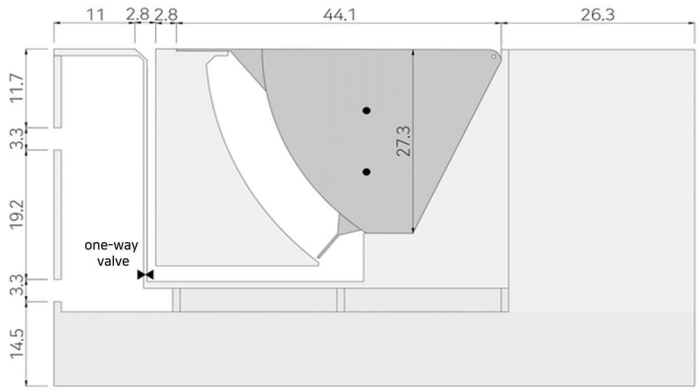

Figure 5. Side view showing the dimensions of the SRFB model (unit: cm). The dark gray areas indicate the movable barrier, while the light gray areas indicate the caisson containing the movable barrier.

Inside the front chamber, two internal waterways are equipped with inlets at a height of 0.47 m (see Figure 3b). Note that the inlet height in the front chamber is higher than the height of the top rectangular holes on the front face of the caisson. Hence, only if the water level in the front chamber exceeds the inlet height of the internal waterway, water from the front chamber starts flowing into the rear chamber through the internal waterway. Another source of water filling the rear chamber comes from the waves overtopping the crest of the caisson, flowing into the inlets of the external waterway located on the top surface of the caisson. At the bottom bend of the internal and external waterway, a one-way check valve

is installed, which allows natural drainage of the water in the rear chamber if the water level in front of the caisson decreases below the elevation of the valve, which is illustrated as the symbol of a black ribbon (See Figure 5).

3.2. Experimental Setup and Measured Quantities

3.2.1. Experiments During Rising or Falling Water Level

The performance of the SRFB was tested by continuously increasing or decreasing the water level without generating waves. To assess the behavior of the flood barrier during water level change, the water depth (h) in front of the caisson gradually increased from 0.35 m to 0.5 m by supplying water to the flume at a constant flow rate, and then decreased back to 0.35 m by draining water from the flume at the same flow rate. The objective of this test was to examine whether the SRFB would rise by buoyancy when the water depth exceeds the elevation of the internal waterway inlet and return to its original position when the water depth falls below the elevation of the one-way valve.

3.2.2. Experiments with Generating Waves

The flood barrier was exposed to regular waves at four different water depths ranging from 0.35 to 0.5 m, with 0.05 m intervals, under varying wave conditions. The incident wave height (H) ranged from 0.05 to 0.2 m with 0.05 m intervals, while the wave period (T) ranged from 1 to 3 s with 1 s intervals. At the water depth of 0.35 m, the highest waves (H = 0.2 m) could not be generated, which prevented the measurement from being conducted. The wave generation time was 60 s for all test conditions.

Ten wave gauges (E01 to E10) were placed to measure the water surface displacement along the wave flume, as shown in Figure 4. Additionally, six pressure transducers (P01 to P06) with a diameter of 10 mm were attached to the front surface of the barrier model to measure the wave pressure exerted on the barrier. The configuration of the pressure transducers is shown in Figure 6. As illustrated, P01–P04 were located on the arc face, whereas P05 and P06 were placed on the parapet supporter and parapet, respectively. All measurements were synchronized and recorded at a frequency of 600 Hz.

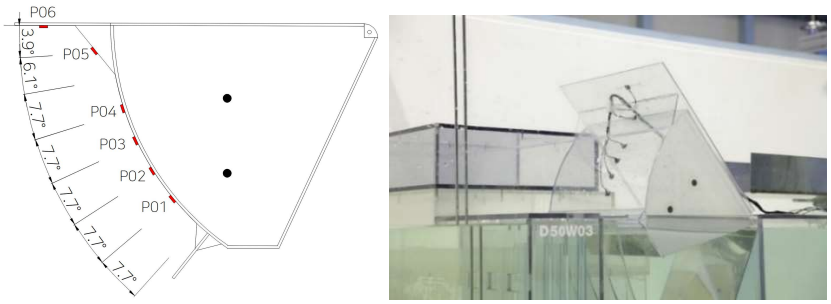

Figure 6. A diagram illustrating the location of the six pressure transducers and a picture showing how they are installed on the model.

Furthermore, the motion of the barrier was tracked by analyzing a video captured during the entire experiment. By calculating the relative displacements of two black circles marked on the side of the model, it was possible to quantitatively evaluate the angular displacement of the flood barrier due to the wave loads. In Figure 7, the relationship between the rotation angle and the standing height is displayed, where R denotes the distance from the hinge to the tip of the parapet, and θ is the rotation angle of the barrier. Thus, the parameter h_R, which denotes the standing height of the barrier, can be expressed as $R \cdot \sin\theta$.

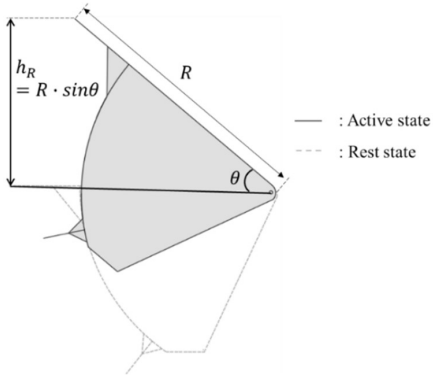

Figure 7. Definition of the standing height of the flood barrier h_R. The shaded areas indicate the shape of the movable barrier when it is in active state.

4. Results

4.1. Variation in Water Level Without Wave Generation

When the water level in the front chamber was lower than the inlet height of the internal waterway (0.47 m), the water in the front chamber did not flow into the rear chamber, and the barrier remained in its rest state. However, when the water level surpassed the internal inlet height, the rear chamber began to fill with water, causing the barrier to rise after some time. Figure 8 shows snapshots taken at four different water depths of h = 0.35 m, 0.4 m, 0.45 m, and 0.5 m, respectively. The barrier stayed within the caisson until the water depth reached 0.45 m, but fully stood up at a depth of 0.5 m. Note that the water level in this condition (h = 0.5 m) is still lower than the crest height of the caisson.

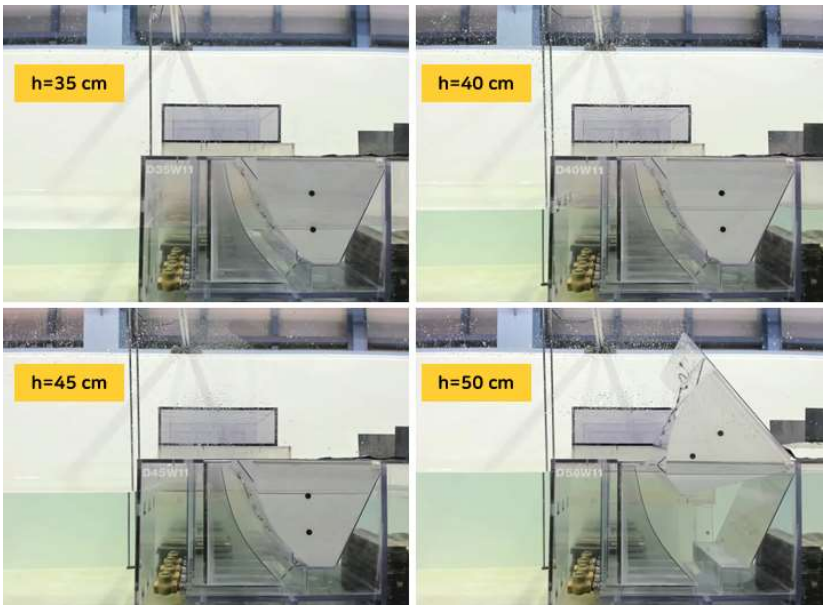

Figure 8. Snapshots of the SRFB model at four different water depths when waves were not generated.

4.2. Generation of Regular Waves with Fixed Water Levels

4.2.1. Time Series of the Measured and Calculated Quantities

Figure 9 presents the experimental result when the wave of H = 0.15 m and T = 3.0 s was applied to the SRFB under a water depth of h = 0.4 m. The result for h = 0.35 m is not provided because there was no movement of the barrier, and, consequently, insignificant pressure measurements were obtained at this water depth. In the figure, the top panel displays the time series of the water surface displacement (η) measured by the wave gauge

in front of the model (E09). The next seven panels correspond to the wave pressures measured by the six pressure transducers (P01 to P06) and the wave force calculated by integrating the measured pressures. The last two panels indicate the rotation angle (θ) and the standing height of the barrier (h_R), estimated by image processing analysis.

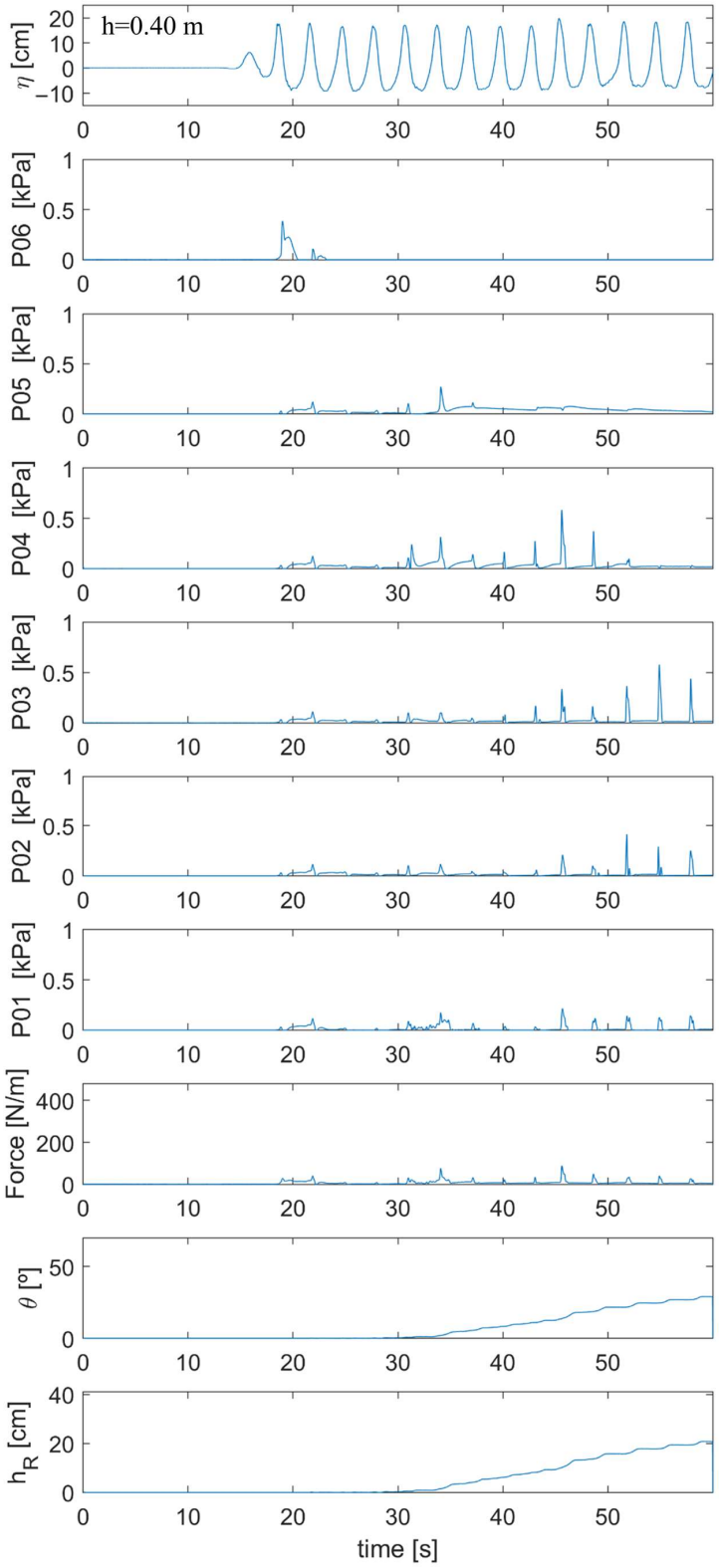

Figure 9. Time series of the water surface displacement, the wave pressures at the six transducers, the rotation angle, and the standing height when h = 0.4 m. The wave condition was H = 0.15 m and T = 3.0 s.

As shown in Figure 9, right after the first one or two waves hit the structure, noticeable pressure was initially measured at the P06 transducer located at the tip of the parapet. This pressure was measured due to the flood barrier being slightly lifted out of position by the impact of the early waves, and then returning to its original position, striking the structure underneath. No further pressure was measured at this transducer afterward. It was observed that the barrier began to slowly rise after approximately the sixth wave impacted the structure. The small wave pressures at P01 to P05 before the barrier was erected were caused by water entering through the gap that flew along the surface of the barrier (see the purple arrow in the left panel of Figure 10). As the barrier rose, the overtopping waves exerted significant pressure on the P02 to P04 transducers located in the middle of the barrier (see the right panel of Figure 10). After 60 s of wave generation had elapsed, the barrier had not fully risen, resulting in only a relatively small pressure being observed at the lowest P01 transducer, which was still positioned inside the rear chamber.

Figure 10. A view of the flood barrier erection during the wave action when h = 0.4 m. The left and right panel shows the appearance after about 40 s and 50 s after wave generation, respectively. The water levels in the rear chamber of the two panels show a clear difference. In the left panel, the yellow and red arrows indicate the flow direction through the internal and external inlets, respectively. The waterway connected to the external inlet is positioned near the glass wall, whereas the waterway connected to the internal inlet is located toward the center of the flume. The purple arrow indicates the water flow falling directly into the rear chamber along the front surface of the flood barrier.

In Figure 11, the results at a water depth of 0.45 m are presented. The description of each panel in the figure is the same as in Figure 9. Under this condition, the flood barrier was raised only after three or four waves hit the structure. At around 45 s, after approximately 10 waves had approached the structure, the barrier fully stood up. The rate of rise in the barrier was significantly faster than in the case of 0.4 m water depth. Even before the barrier was fully raised, all pressure transducers recorded pressure as water entered the rear chamber through the internal and external inlets. Water was also entering through the gap between the tip of the barrier and the top of the caisson, causing pressure readings at the P05 and P06 transducers at early times. As the barrier rose, progressively larger pressures were exerted on the lower pressure transducers, with the highest pressure of about 1 kPa recorded at the P01 transducer just before the barrier was fully raised (see Figure 12). Once the barrier fully stood up, no more waves reached the pressure transducers on the upper locations, and only the two lowest transducers (P01 and P02) experienced relatively smaller wave pressures.

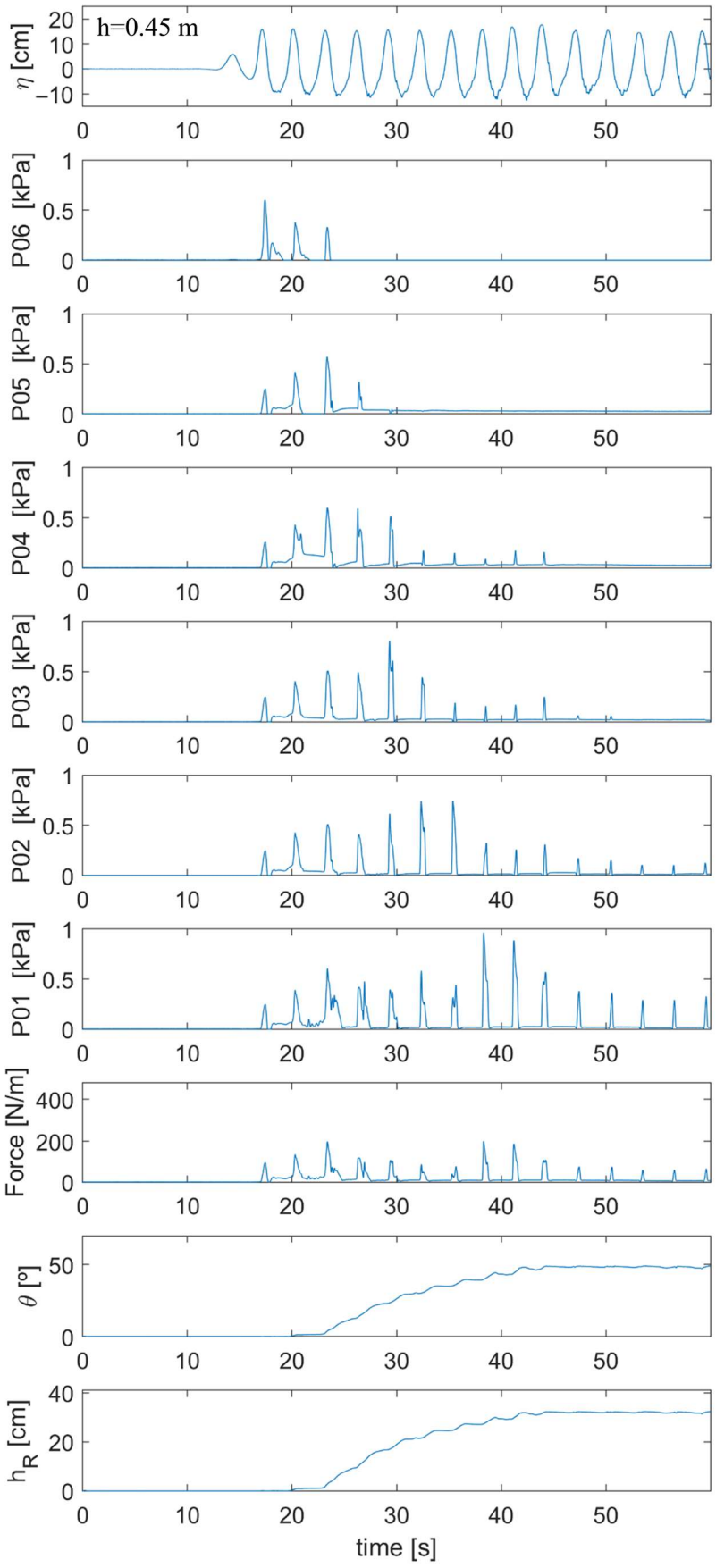

Figure 11. Time series of the water surface displacement, the wave pressures at the six transducers, the rotation angle, and the standing height when h = 0.45 m. The wave condition was H = 0.15 m and T = 3.0 s.

Figure 12. A view of the flood barrier erection during the wave action when h = 0.45 m. The barrier was almost fully erected. The wave hit the front face of the barrier, causing significant pressure to be applied on the pressure transducers located there.

In Figure 13, the results for h = 0.5 m are shown. In this condition, the still water level was higher than the elevation of the inner inlet (0.47 m), so the measurements were taken with the flood barrier already fully raised before the waves were generated. Consequently, the rotation angle and the standing height of the barrier remained constant during the measurement. The highest pressure, close to 1 kPa, was measured at the P01 transducer, as the overtopping waves mainly impacted the lower section of the barrier. The measured pressures decreased as the transducer elevation increased. The uppermost P06 transducer, located on the parapet of the barrier, had no water contact, resulting in no pressure being measured. Since the barrier did not move during the measurement, the pressure magnitudes at all the transducers and the resulting wave forces changed minimally over time.

Wave pressure exerted on a structure can be categorized into two types: quasi-static or pulsating pressure and impulsive pressure [23]. Quasi-static wave pressure can be scaled using the Froude similarity law without requiring adjustments for scaling effects. In contrast, impulsive wave pressure acts over an extremely short duration, less than 1/100 of the wave period, and is influenced by air effects that do not conform to Froude similarity. Therefore, its magnitude should be corrected using appropriate adjustment methods. As shown in Figures 9, 11 and 13, the wave pressure acting on the SRFB lasts significantly longer than 1/100 of the wave period and thus corresponds to quasi-static pressure. Consequently, the measured wave pressure can be directly scaled using the Froude similarity law. In the above, explanations are presented only for the longest wave period (T = 3 s) with the same wave height (H = 0.15 m) under different water depth conditions. When the wave height was the same and the wave period was smaller, the magnitude of wave pressures on the barrier was similar, but the time required for the barrier to stand up was longer, and the final standing angle was also reduced.

Another noteworthy thing is that once wave overtopping begins, the flood barrier quickly rises after the first few waves hit, thereby preventing further overtopping. During the physical experiments, measurement equipment was installed behind the caisson to measure the volume of wave overtopping, which was found to be less than 0.01 $m^3/s/m$ for all the test cases. This value is well within the allowable wave overtopping rate for conventional seawalls, indicating that the flood barrier effectively prevents wave overtopping.

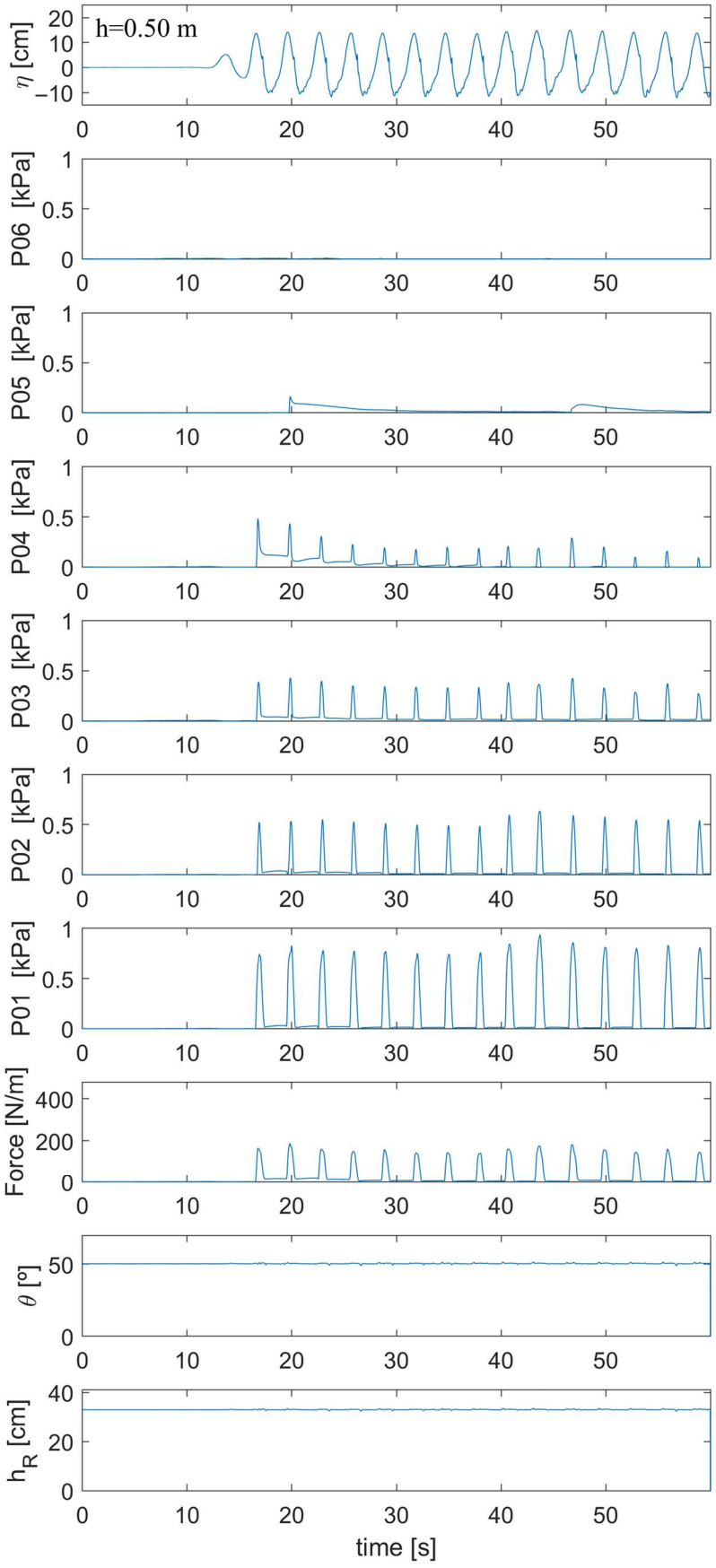

Figure 13. Time series of the water surface displacement, the wave pressures at the six transducers, the rotation angle, and the standing height when h = 0.5 m. The wave condition was H = 0.15 m and T = 3.0 s.

4.2.2. Distributions of Instantaneous Pressures on SRFB

Since the wave pressures acting on the front face of the flood barrier changed during the rise in the barrier, the instantaneous wave pressures at a particular rotation angle were also constantly changing. As illustrated in the above section, the range of movement is greatest when h = 0.45 m. Hence, the variation in the instantaneous wave pressures with the rotation angle was examined for this condition. Figure 14 presents snapshots of the pressure distribution along the front face of the barrier at rotation angles of θ = 0°, 15°, 30°, and 45° during its upward movement, under the wave condition of H = 0.15 m and T = 3 s. In the figure, the lower x-axis denotes the magnitude of pressure, while the upper x-axis represents the horizontal length scale measured from the vertical front wall of the caisson. The y-axis represents the vertical length scale measured from the floor of the wave flume. The direction of the pressure acting on each transducer is displayed perpendicular to the surface of the barrier.

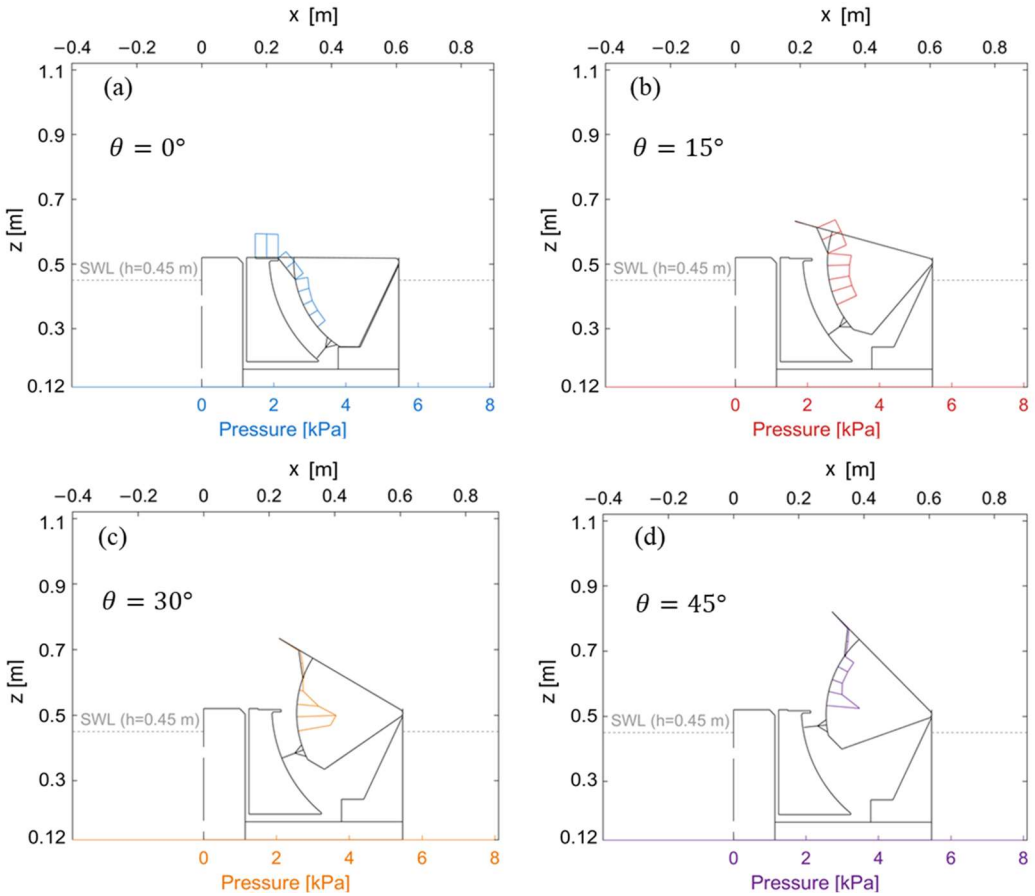

Figure 14. Distributions of the instantaneous pressures along the front face of the flood barrier at four different rotation angles when h = 0.45 m, H = 0.15 m, and T = 3 s. The upper and left axes of each panel show the distance in the horizontal and vertical directions measured from the front face and the crest height of the caisson, respectively. The scale shown at the bottom of the panel illustrates the magnitude of the wave pressure: (**a**) θ = 0°; (**b**) θ = 15°; (**c**) θ = 30°; (**d**) θ = 45°. In each figure, the instantaneous pressures are displayed in different colors according to different rotation angles.

As shown in Figure 14a, even before the barrier began to rise, noticeable pressures were observed at the parapet section of the barrier, while smaller pressures were measured at the transducers positioned lower down. This occurred because water from overtopping waves flowed through the thin gap between the top of the caisson and the tip of the barrier, as illustrated in Figure 11. Water entering through the gap fell into the empty space in

front of the barrier's front face and dropped into the water contained in the rear chamber. During this process, some pressure was exerted on the transducer located on the parapet support (P02). Meanwhile, the pressures on the arc-shaped surface of the barrier resulted from the dynamic fluctuation of the water level in the rear chamber, as these sections were already immersed in the water before the measurement began.

Figure 14b depicts the pressure distributions at $\theta = 15°$. The wave pressures acting on both the arc-shaped face and the parapet support were distributed close to evenly. However, there was a slight decrease in the magnitude of the wave pressure towards the bottom of the barrier. In this condition, the gap between the flood barrier and the top of the caisson widened significantly, preventing overtopping waves from passing behind the barrier. Instead, these waves freely fell into the rear chamber after striking the barrier, resulting in much higher pressures along the barrier compared to those at $\theta = 0°$. The pressures measured at the arc-shaped section of the barrier result from a combination of the hydrodynamic pressures due to the displacement of the barrier relative to the rising water level in the rear chamber, as well as the impact of overtopping waves striking the barrier. The parapet supports experienced similar wave pressures to the arc-shaped section of the barrier. However, minimal wave pressure was measured at the uppermost parapet, indicating water could not reach this location even when $\theta = 15°$.

Figure 14c illustrates the pressure distribution at $\theta = 30°$, where the barrier has reached approximately 60% of its maximum standing height. As shown in the figure, the pressures were far from evenly distributed. Higher pressures were measured on the lower section of the barrier as the overtopping water flows into the rear chamber, while less significant pressures were measured on the upper section of the barrier. This phenomenon occurred because the overtopped water flew along the barrier surface into the rear chamber, exerting strong pressure on the lower part of the barrier, as shown in the right panel of Figure 10. At this rotation angle, only very weak pressures were detected on the parapet support, which was caused by the light contact of the water returning from the front face of the barrier.

Figure 14d shows the results at $\theta = 45°$. As the barrier rose nearly to its maximum standing height, significant pressures were exerted on the lower section of the barrier, coinciding with the arrival of overtopping waves. Synchronized video revealed that most of the incoming water could not flow into the rear chamber due to its limited storage capacity. Instead, the water climbed up along the arc-shaped front face of the barrier and then naturally descended due to gravity. The parapet and the support underneath remained almost unaffected by the impact of overtopping waves.

4.2.3. Variation in Pressures Depending on the Water Level and Rotation Angle

When designing a flood barrier, it is crucial to understand the maximum wave force as the barrier rises. Figure 15 provides this information by showing the instantaneous pressure distribution corresponding to the maximum wave force on the barrier under two different water depth conditions. The result for $h = 0.4$ m, as shown in Figure 15a, illustrates the pressure distribution when the maximum load $F_{max} = 88.6$ N/m was applied. At that time, the barrier's rotation angle was $\theta_{F_{max}} = 14°$. The figure indicates that the upper section of the arc-shaped barrier experienced high pressures due to the impact of the overtopping waves, predominantly affecting this area. Figure 15b presents the pressure distribution for $h = 0.45$ m, where the maximum wave force $F_{max} = 200.9$ N/m acted at a rotation angle of $\theta = 40°$. In this case, much stronger pressures were exerted over a narrow range of the barrier, slightly above and below the crest height of the caisson. The parapet of the barrier experienced only minimal pressures in both figures, suggesting insignificant wave runup at that point at the moment of maximum wave load.

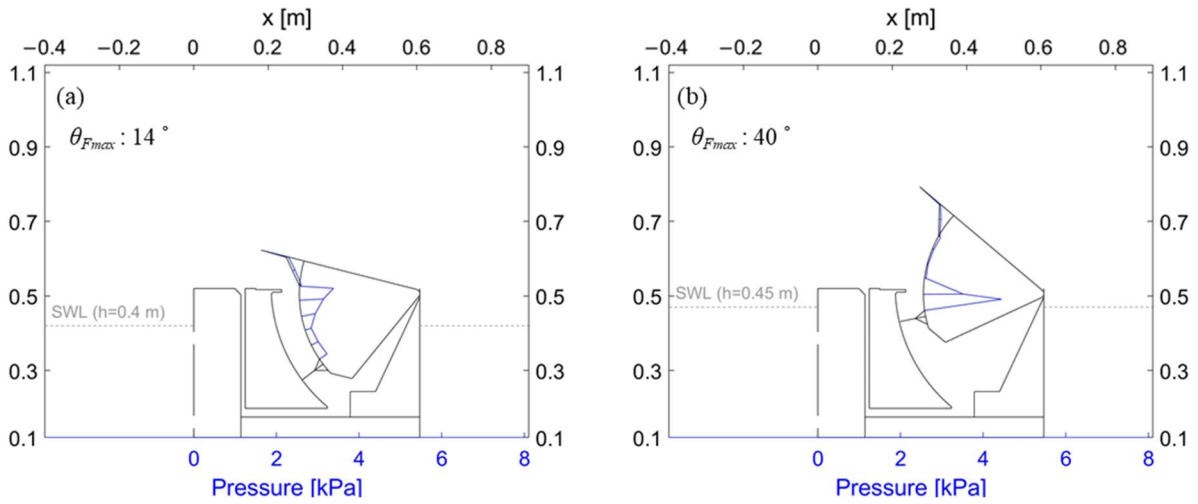

Figure 15. Instantaneous pressure distributions when the maximum wave force acting on the front face of the flood barrier: (**a**) h = 0.4 m; (**b**) h = 0.45 m. The wave condition was H = 0.15 m and T = 3 s for both cases.

Figure 16 illustrates how the peak wave force acting on the entire flood barrier changed with the rotation angle (θ) for h = 0.4 m and 0.45 m. The peak wave force is denoted by F_p, which represents the local maximum values of wave forces acting on the SRFB. The wave forces have been presented in the eighth panel from the top in Figures 9 and 11 for h = 0.4 m and 0.45 m, respectively, while the rotation angle values are shown in the ninth panel. When individual waves act repeatedly, the local maximum values of wave forces and the corresponding rotation angles at which these peaks occur can be extracted and represented as shown in Figure 16. Note that only data recorded after the barrier began to rise were included in Figure 16. Over the 60 s observation period, peak wave forces appeared two times in both cases at θ = 2.2° and 13.7° for h = 0.4 m, whereas θ = 3.5° and 39.8° for h = 0.45 m. The correlation between these peak forces and the rotation angles of the flood barrier is found in Figure 16.

In Figure 16a, the rotation angle range varied because the final stand-up position of the flood barrier differed between the conditions of h = 0.4 m and 0.45 m. As shown in the figure, significant fluctuations in wave force appeared during the rising motion of the barrier. Overall, the peak forces at h = 0.4 m were notably lower than those at h = 0.45 m, a result also found in Table 1, which presents the mean and standard deviations of the peak wave forces for different water depths. When h = 0.35 m and 0.5 m, the flood barrier did not move during the measurements, so these cases are not represented in Figure 15. However, the mean and standard deviations of the peak forces for these depths are provided in Table 1. When the water depth was 0.35 m, very weak wave forces were measured even though the barrier was not erected. This was because the overtopped water seeped through the narrow space between the tip of the barrier and the top surface of the caisson located below it, flowed down along the front face of the barrier, and soaked the pressure transducers.

Table 1. Values of the mean and standard deviation of the peak wave forces at different water depths.

	h = 0.35 m	h = 0.4 m	h = 0.45 m	h = 0.5 m
Mean (μ) [N/m]	5.6	37.2	112.1	158.2
Standard deviation (σ) [N/m]	3.2	22.3	48.4	14.5

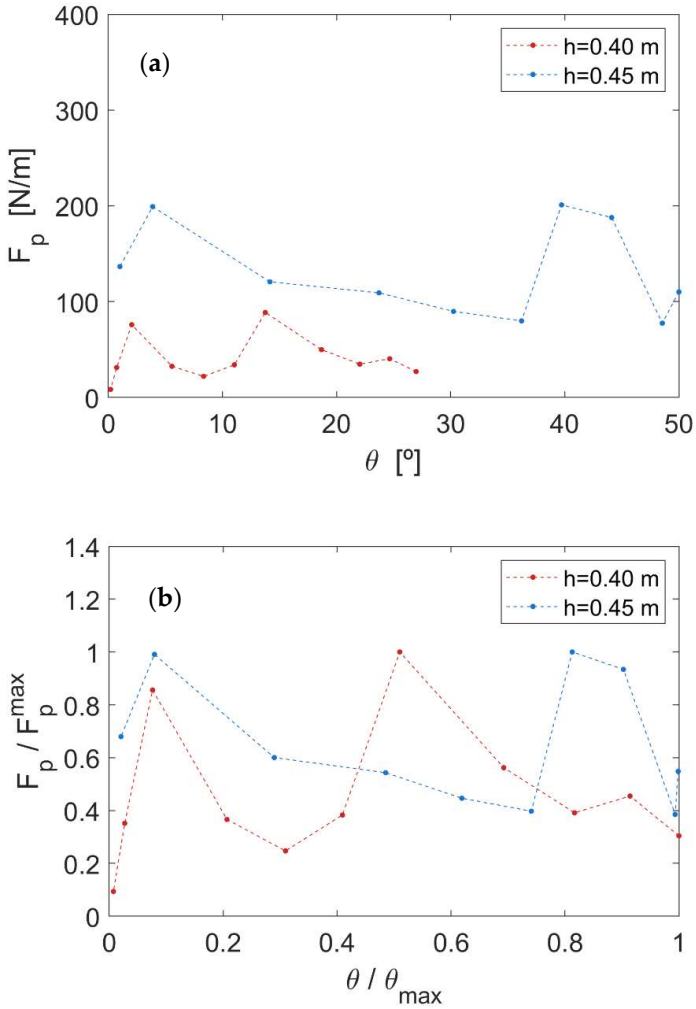

Figure 16. Variation in the peak wave forces along the rotation angle. (**a**) Dimensional results; (**b**) dimensionless results.

Meanwhile, Figure 16b presents the same data in a dimensionless format. In this figure, the peak wave forces (F_p) are normalized by the maximum wave force (F_p^{max}) and shown as a dimensionless rotation angle at a specific time, divided by the maximum rotation angle (θ_{max}). Notably, relatively large dimensionless wave forces were observed around $\theta/\theta_{max} = 0.1$ for both water depths, indicating that substantially large wave forces were applied to the barrier during the initial stage of its rise. This is due to a significant amount of water flowing over the crest of the caisson and striking the barrier before entering the rear chamber. A second peak in wave forces appeared around $\theta/\theta_{max} = 0.5$ for $h = 0.4$ m, and $\theta/\theta_{max} = 0.8$ for $h = 0.45$ m. The magnitudes of these normalized forces were nearly the same as those observed at $\theta/\theta_{max} = 0.1$.

Description of the experimental results in the above focused on the specific wave condition of $H = 0.15$ m and $T = 3$ s, representing the longest wave period and the second largest wave height among the test waves. Figure 17 presents more comprehensive results, showing the mean values of peak wave forces for different water depths and wave heights with the same wave period. As indicated in Figure 17a, the mean peak wave force (F_p^{mean}) acting on the flood barrier was relatively small at the shallowest water depth ($h = 0.35$ m). The values generally increased as the water depth increased, but did not rise significantly with increasing water depth with the smallest wave condition ($H = 0.05$ m).

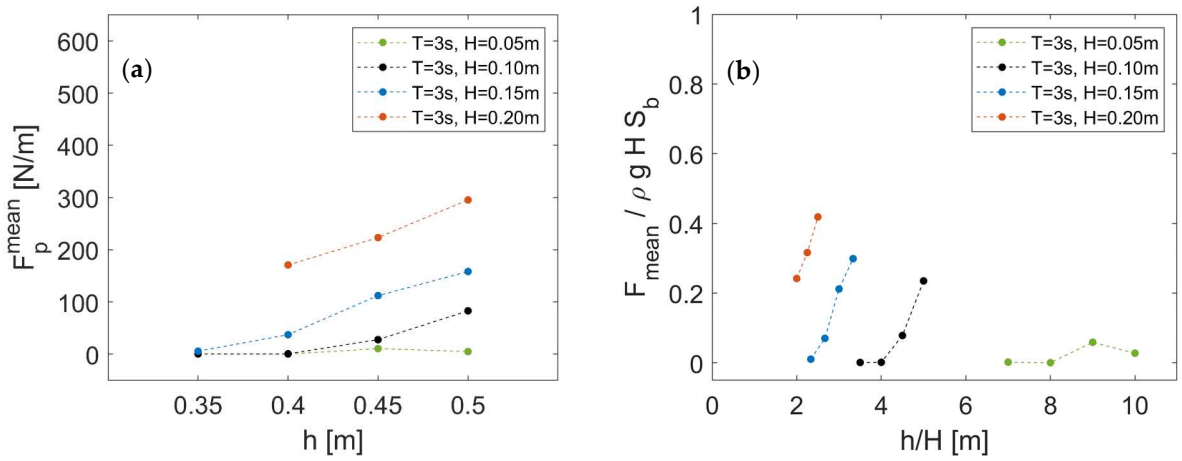

Figure 17. Variation in the mean peak wave forces for different water depths with various wave heights. (**a**) Dimensional results; (**b**) dimensionless results.

Figure 17b presents the results from Figure 17a in a dimensionless form. The x-axis represents the ratio of water depth (h) to wave height (H), while the y-axis is expressed as $F_p^{mean}/\rho gHS_b$, where ρ is the density of water, g is gravitational acceleration, and S_b is the total length along the flood barrier surface covered by the six pressure transducers. In general, wave pressure acting on coastal structures is often nondimensionalized as $p/\rho gH$. For example, the well-known Goda's formula [24], commonly used to calculate the wave pressure on vertical walls, can be expressed as $p = C\rho gH$, where C is a parameter determined by wave conditions, the location of wave action, and the geometry of the structure. Within this context, the wave force per unit width can be normalized by dividing the nondimensionalized wave pressure by the vertical distance at which it acts. For the case of the SRFB, this can be expressed as $F_p^{mean}/\rho gHS_b$. As shown in Figure 17b, a lower h/H value generally corresponds to a higher upper limit of the dimensionless wave force. Nevertheless, the maximum value of $F_p^{mean}/\rho gHS_b$ remains well below unity, indicating that the wave force acting on the SRFB is significantly lower than Goda's estimates that predict $p/\rho gH \approx 1$ or greater when design waves impact vertical walls. It is noteworthy that greater wave heights than those tested in this experiment could produce higher wave pressures. Similarly, irregular waves may result in larger wave forces. However, it is clear that no impulsive wave pressures exceeding the predictions of Goda's formula were observed in this study.

Figure 18 presents the results of the maximum peak wave force (F_p^{max}) for the same experimental conditions as Figure 17. These values represent the largest wave force acting on the flood barrier during the 60 s measurement period under each test condition. The overall trend observed in Figure 18a was similar to that in Figure 18b, although under certain conditions, the maximum force was higher at h = 0.45 m than h = 0.5 m. The results shown in Figure 18b also exhibit trends similar to those in Figure 18a, with values generally slightly higher. The largest maximum force among all test conditions was 410 N/m, which corresponds to a nondimensionalized value of $F_p^{max}/\rho gHS_b$ = 0.57. However, impulsive pressure may occur under certain conditions, especially when large irregular waves act on SRFB. Therefore, conducting further experiments is recommended to better understand the magnitude and distribution pattern of wave pressures along the flood barrier for optimal structural design.

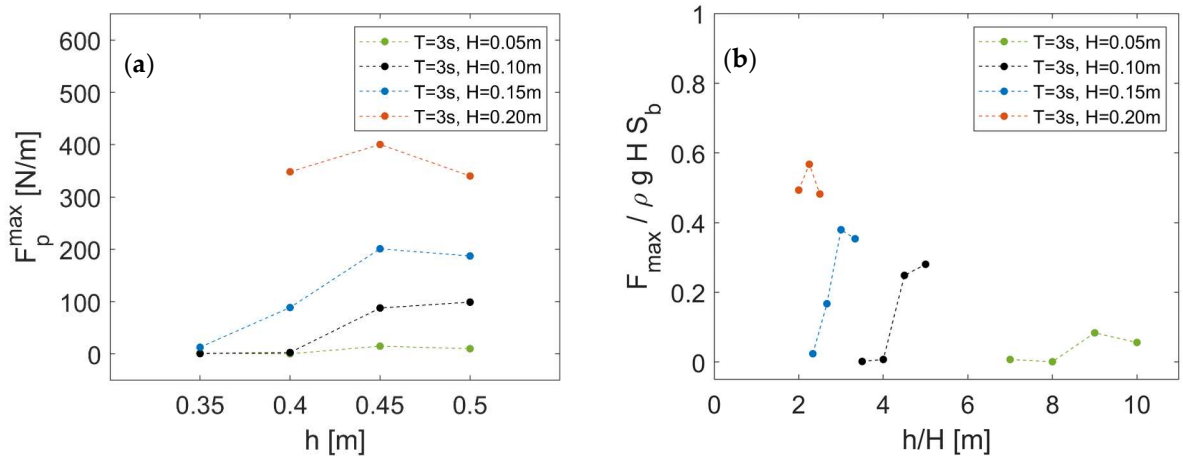

Figure 18. Variation in the maximum peak wave forces for different water depths with various wave heights. (**a**) Dimensional results; (**b**) dimensionless results.

5. Conclusions

This study presents the fundamental principles and hydraulic characteristics of the self-rotating flood barrier (SRFB) by conducting physical experiments in a wave flume. The SRFB is designed to selectively rise only under specific conditions when the water level exceeds a certain threshold or wave overtopping occurs. During periods of low risk, the flood barrier remains concealed within an underground caisson, allowing unobstructed enjoyment of the landscape and view. Structurally, the SRFB resembles a radial gate, conveying externally applied forces to its hinge. However, its operation is entirely buoyancy-driven, eliminating the need for external power or manual intervention. The threshold for the barrier's activation and return can be customized to the local sea conditions by adjusting the elevation, number, and size of internal and external inlets.

Experiments conducted under conditions of changing water levels without wave action demonstrated that the SRFB model remained concealed within its caisson unless the water entered the rear chamber housing the flood barrier. In contrast, once the water level or wave conditions caused water to flow into the rear chamber through either internal or external inlets, the barrier rapidly deployed, effectively preventing water from passing behind it. The time it took for the barrier to begin rising and the speed of its ascent varied depending on the freeboard and wave conditions. It was also confirmed that the SRFB model returned to its original position when the water level dropped below the elevation of the one-way valve.

If the amount of water entering through the internal and external inlets, along with the waters overtopping the crest height of the caisson, was relatively small, the pressure on the barrier remained insignificant. However, once the barrier rose to a sufficient height to resist wave action, it encountered noticeable pressure. The pressure distribution on the front face of the barrier varied with the rotation angle, with the highest pressures appearing slightly above and below the crest height of the caisson. Based on detailed analysis, the specific angle at which the peak wave force was applied and the resulting pressure distribution were clearly identified. The magnitudes of the peak wave forces acting on the flood barrier are also compared for different experimental conditions, which will be useful for the design of this structure.

In this study, the SRFB model was made of acrylic, but a prototype structure would be made of heavier materials such as steel. Therefore, the buoyancy forces and the behavioral characteristics of the flood barrier under its influence may differ from the results of the present experiment. In light of this, further design review may be required, either through

additional numerical modeling or larger-scale physical experiments. In addition, if some silt, sand, or dirt enters the chambers, they are likely to get stuck around the moving parts of the barrier, causing the barrier to fail. Hence, the actual design needs to be improved to allow for better drainage of these materials. This could be accomplished by sloping the bottom of the caisson slightly toward the offshore, or by installing suitably robust screens at the inlets to prevent floating debris from entering the chamber too easily. It may also require periodic cleaning and maintenance. Further complementary studies should be conducted in the future, focusing on these aspects.

In addition, further experiments using irregular waves are necessary for future studies to investigate more realistic behavior and the resulting forces exerted on the SRFB. During the flood barrier rising process, the increase in both the rotation angle and the standing height will vary irregularly. Above all, wave irregularity will increase the fluctuations of local peak pressures on the structure. Unlike regular waves, some irregular wave trains are inconsistent and tend to focus and break more quickly before reaching the SRFB. In such cases, overtopping waves may carry a large momentum flux that generates greater impact pressures, especially when smaller waves superpose onto a larger wave immediately before the SRFB.

Author Contributions: Conceptualization, S.-H.O.; methodology, J.L. and S.-H.O.; software, J.L.; validation, J.L. and S.-H.O.; formal analysis, J.L. and B.N.; investigation, J.L., B.N., and S.-H.O.; data curation, J.L.; writing—original draft preparation, J.L. and B.N.; writing—review and editing, S.-H.O.; project administration, S.-H.O.; funding acquisition, S.-H.O. All authors have read and agreed to the published version of the manuscript.

Funding: This research was funded by a research project titled "Development of Advanced Technology for Ocean Energy, Harbor and Offshore Structure", which was funded by Korea Institute of Ocean Science and Technology (Project No. PEA 0321). The corresponding author was supported by the Basic Science Research Program through the National Research Foundation of Korea (NRF) funded by the Ministry of Education (No. 2022R1F1A1069313).

Data Availability Statement: The data presented in this study are available on request from the corresponding author.

Conflicts of Interest: The authors declare no conflicts of interest.

References

1. Woodruff, J.D.; Irish, J.L.; Camargo, S.J. Coastal flooding by tropical cyclones and sea-level rise. *Nature* **2013**, *504*, 44–52. [CrossRef] [PubMed]
2. Wu, G.; Shi, F.; Kirby, J.T.; Liang, B.; Shi, J. Modeling wave effects on storm surge and coastal inundation. *Coast. Eng.* **2018**, *140*, 371–382. [CrossRef]
3. Kimura, Y.; Mase, H. Numerical simulation of a rising seawall for coastal flood protection. *J. Waterw. Port Coast. Ocean Eng.* **2014**, *140*, 04014002. [CrossRef]
4. Walraven, M.; Vrolijk, K.; Kothuis, B.B. Design, maintain and operate movable storm surge barriers for flood risk reduction. In *Coastal Flood Risk Reduction*; Elsevier: Amsterdam, The Netherlands, 2022; pp. 271–286.
5. Seifert, R.E.; Moore, J.W. Floodgate operations and fish communities in tidal creeks of the lower Fraser River (British Columbia, Canada). *Estuaries Coasts* **2018**, *41*, 1206–1221. [CrossRef]
6. Mel, R.A.; Viero, D.P.; Carniello, L.; D'Alpaos, L. Optimal floodgate operation for river flood management: The case study of Padova (Italy). *J. Hydrol. Reg. Stud.* **2020**, *30*, 100702. [CrossRef]
7. PIANC. *Design of Movable Weirs and Storm Surge Barriers: Report of Working Group 26 of the Inland Navigation Commission*; Brussels, Belgium, 2006. Available online: https://www.pianc.org/publication/design-of-movable-weirs-and-storm-surge-barriers/ (accessed on 5 August 2025).
8. Mooyaart, L.F.; Jonkman, S.N. Overview and design considerations of storm surge barriers. *J. Waterw. Port Coast. Ocean Eng.* **2017**, *143*, 06017001. [CrossRef]

9. Kirshen, P.; Borrelli, M.; Byrnes, J.; Chen, R.; Lockwood, L.; Watson, C.; Starbuck, K.; Wiggin, J.; Novelly, A.; Uiterwyk, K.; et al. Integrated assessment of storm surge barrier systems under present and future climates and comparison to alternatives: A case study of Boston, USA. *Clim. Chang.* **2020**, *162*, 445–464. [CrossRef]
10. Takagi, H.; Tomiyasu, R.; Araki, T.; Oyake, T.; Asakawa, N.; Ishihara, I.; Kawakoa, T.; Yan, F.; Kokusho, H.; Hino, M. Feasibility of a self-powered movable seawall using microtidal energy in Japan. *Renew. Energy* **2023**, *219*, 119563. [CrossRef]
11. Tieleman, O.C.; Hofland, B.; Tsouvalas, A.; de Almeida, E.; Jonkman, S.N. A fluid–structure interaction model for assessing the safety of flood gate vibrations due to wave impacts. *Coast. Eng.* **2021**, *170*, 104007. [CrossRef]
12. Marissen, R.; Mulder, J.S.; Wienke, D.; Bergsma, O. Design considerations on a flexible membrane tsunami flood barrier. *Mater. Sci. Appl.* **2013**, *4*, 846–855. [CrossRef]
13. Ianakiev, A.; Greenwood, J. Design and analysis of rotomoulded panels for a self-erecting low-cost flood barrier. *Archit. Eng. Des. Manag.* **2013**, *9*, 110–120. [CrossRef]
14. Sammarco, P.; Fischione, P.; Romano, A.; Bellotti, G.; Dalla Villa, S. Prototype data analysis of the dynamics of the Venice gate-barriers during an extreme storm event. *Coast. Eng.* **2024**, *194*, 104623. [CrossRef]
15. Alberti, T.; Anzidei, M.; Faranda, D.; Vecchio, A.; Favaro, M.; Papa, A. Dynamical diagnostic of extreme events in Venice lagoon and their mitigation with the MoSE. *Sci. Rep.* **2023**, *13*, 10475. [CrossRef] [PubMed]
16. Mugesh, A.; Krishnan, L.; Kumar, S.P.; Salem, S.S. Self-closing flood barrier: A preventive system to defense extreme high flood events. *Int. J. Eng. Res. Technol.* **2015**, *4*, 602–604.
17. Self-Closing Flood Barrier. Available online: https://selfclosingfloodbarrier.com/ (accessed on 31 July 2024).
18. Kimura, Y.; Wakunaga, T.; Yasuda, M.; Kimura, H.; Kani, N.; Mase, H. Development and verification of wall-flap-gate as tsunami inundation defence for nuclear plants. *Nucl. Eng. Des.* **2017**, *323*, 299–308. [CrossRef]
19. Stagonas, D.; Ravindar, R.; Sriram, V.; Schimmels, S. Experimental evidence of the influence of recurves on wave loads at vertical seawalls. *Water* **2020**, *12*, 889. [CrossRef]
20. Oh, S.H.; Jang, S.C.; Lee, J. Wave overtopping and loading for the recurved parapets on the crest of rubble mound breakwater. In *Coasts, Marine Structures and Breakwaters 2017: Realising the Potential*; ICE Publishing: London, UK, 2018; pp. 979–985.
21. Oh, S.H.; Lee, D.S. Two-dimensional wave flume with water circulating system for controlling water level. *J. Korean Soc. Coast. Ocean Eng.* **2018**, *30*, 337–342. [CrossRef]
22. Lykke Andersen, T.; Clavero, M.; Firgaard, P.; Losada, M.; Puyol, J.I. A new active absorption system and its performance to linear and non-linear waves. *Coast. Eng.* **2016**, *114*, 47–60. [CrossRef]
23. Cuomo, G.; Allsop, W.; Takahashi, S. Scaling wave impact pressures on vertical walls. *Coast. Eng.* **2010**, *57*, 604–609. [CrossRef]
24. Goda, Y. New wave pressure formulae for composite breakwaters. In Proceedings of the 14th Coastal Engineering Conference, Copenhagen, Denmark, 24–28 June 1974; American Society of Civil Engineers: New York, NY, USA, 1975; pp. 1702–1720.